

MODAL DECOMPOSITION OF SPACECRAFT RELATIVE MOTION IN QUASI-PERIODIC ORBITS

Ethan R. Burnett* and Hanspeter Schaub†

This paper develops new tools for close-proximity spacecraft relative motion guidance in slowly varying or quasi-periodic orbits in highly perturbed environments. The task of designing safe relative motion in this context is achieved using transformations of the linearized relative motion dynamics in differential orbit elements, generated from a high-fidelity model. Notably, the periodic part of the time-varying plant matrix is sampled over a quasi-period via Fourier transformations, and used to obtain modal decompositions in a transformed space for which the dynamics are linear time-invariant (LTI). As the spacecraft orbits evolve, the Fourier coefficients of the periodic component of the plant matrix change, the most robust relative motion modes change only slowly, and the effects of the non-periodic part of the plant matrix are secondary. Thus, only small corrective maneuvers are needed for a spacecraft to continually follow sufficiently close to a desired modal motion.

INTRODUCTION

For spacecraft in close proximity to one another in unperturbed orbits, the relative position and velocity of one spacecraft with respect to the other can be described via analytic equations in terms of initial relative state conditions, constants obtained from the spacecraft orbit elements and differences, and an independent variable such as time or the true anomaly of one of the spacecraft.^{11,21,27,28} The simplicity of these formulations has facilitated an elegantly simple design of non-drifting spacecraft relative motion using the natural solutions of the unperturbed differential dynamics.²⁴ In addition, small maneuvers may be used in combination with the natural motion to achieve more complex control goals, again facilitated by the fact that the relative motion is well-understood.

There is great interest in the formation flying and spacecraft rendezvous planning communities for understanding the nature of relative motion under the influence of various orbital perturbations. In support of this interest, the dynamics of perturbed relative motion have been very well-studied. Works have examined the influence of perturbations from higher-order components of the gravitational potential,^{8,20,23} differential drag,¹⁸ and differential solar radiation pressure.^{9,16} In some cases, analytic approaches provide concise and useful information for formation design in the presence of common perturbations. For example, for relative motion in the J_2 potential, Reference 23 analytically describes the first-order conditions for non-drifting relative motion. The simplicity in

*Research Assistant, NDSEG Fellow, Ann and H.J. Smead Department of Aerospace Engineering Sciences, University of Colorado Boulder, Boulder, CO, 80309 USA.

†Glenn L. Murphy Chair of Engineering, Smead Department of Aerospace Engineering Sciences, University of Colorado, 431 UCB, Colorado Center for Astrodynamics Research, Boulder, CO 80309-0431. AAS Fellow, AIAA Fellow.

formation design for unperturbed orbits can thus be inherited to some degree in cases with of the addition of a few perturbations.

For spacecraft motion in highly perturbed environments, such as in asteroid or moon orbits, the dynamics are so complicated that the relevant analytic relative motion models are exceedingly complex, and concise analytic expressions illustrating the types of motion and conditions with zero drift are very difficult to obtain. Due to the high degree of complexity and uncertainty, the task of robust long-term formation design or rendezvous and circumnavigation guidance in these environments will often require that the problem be addressed numerically, at least in part. A highly relevant numerical analysis of perturbed relative motion can be found in Reference 4, which studies bounded relative orbits about slowly rotating asteroids. The dynamics in that paper are two-body gravity perturbed by the C_{20} and C_{22} coefficients, which are typically the two dominant terms in an asteroid gravity field. The work computes periodic orbits and associated quasi-periodic invariant tori, and uses the resulting structure to identify bounded relative motion conditions. Additionally, Reference 3 advances a similar bounded relative motion goal but for the full zonal problem.

This paper differs from prior works by providing a framework for characterization of the many types of useful close-proximity relative motion that can be achieved in a variety of perturbed orbits, with a systematic and computationally feasible approach. Using this approach, there is extensive opportunity for a readily comprehensible exploration of the relative motion for two spacecraft in nearby quasi-periodic or slowly-varying perturbed orbits. It relies on the fact that for such orbits, the local linearized relative motion dynamics will have an almost-periodic plant matrix. In other words, over some interval of time, the dynamics of the local relative state of two nearby spacecraft \mathbf{x} will obey the linearization $\dot{\mathbf{x}} = [A(t)]\mathbf{x}$, where $[A(t)] \approx [A(t + T)]$ for some quasi-period T .

Previous work in Reference 10 explores deriving and using linear dynamic approximations of the highly perturbed formation dynamics. In cases where the plant matrix is exactly periodic, it is possible to perform a modal decomposition of the spacecraft relative motion behavior using tools from Floquet theory. The modal decomposition is a useful description because the linear relative motion dynamics behave as a superposition of stable or unstable relative motion modes. Close-proximity perturbed relative motion in this context can thus be described as a linear combination of independent modes that can be individually investigated. Studying the problem through the lens of modal decomposition allows for straightforward formation design and control techniques, despite the high degree of dynamical complexity.

This paper analyzes systems with almost-periodic plant matrices in a manner that explicitly accounts for the effects of non-periodicity of the plant matrix. For a system with almost-periodic plant matrix $[A(t)]$, the nearest periodic matrix $[\bar{A}(t)] = [\bar{A}(t + T)]$ can be found, yielding a similar dynamical system to the original, but for which a modal decomposition can be computed. Conditions for a given motion predicted by this decomposition to be closely followed in the original system are discussed. Importantly, using the modal decompositions, accurate guidance solutions for long-term low-control effort bounded relative motion may be identified, even when the orbital dynamics are highly complicated. This is demonstrated for the problem of formation design in quasi-periodic terminator orbits around the asteroid 162173 Ryugu. This paper also devises a preliminary guidance and control implementation for computing and targeting relative motion modes. It is designed to be computationally feasible and reasonably robust to dynamical uncertainty and imprecise knowledge of the exact formation orbital conditions, requiring only the ability to estimate spacecraft relative positions and velocities to high precision. For some missions, it will be a superior alternative to a continuous feedback-based formation control strategy.

CONCEPTUAL BASIS AND BACKGROUND

Mode Targeting Fundamentals

The main idea of a mode targeting strategy is to identify the initial conditions for a desired relative motion modal behavior, control to them, and then follow the natural dynamics for the limited timespan of accuracy of the prediction, before correcting the spacecraft motion to follow updated desired mode conditions. The fundamental modal behaviors serve as the building blocks for any desired admissible relative motion behavior, and the guidance implementation mitigates errors from small dynamic and navigational uncertainties, as well as dynamic inaccuracies from non-periodicity of the plant matrix, via small planned short-duration corrective maneuvers. The frequency of these maneuvers depends on the scale of non-periodic terms in the plant matrix, the level of dynamic uncertainty, and the level of state uncertainty. A major benefit of this approach is that instead of fighting the dominant perturbations and wasting fuel, the perturbed dynamics are partially exploited for formation-keeping or rendezvous, because they determine the shape of the resulting trajectories.

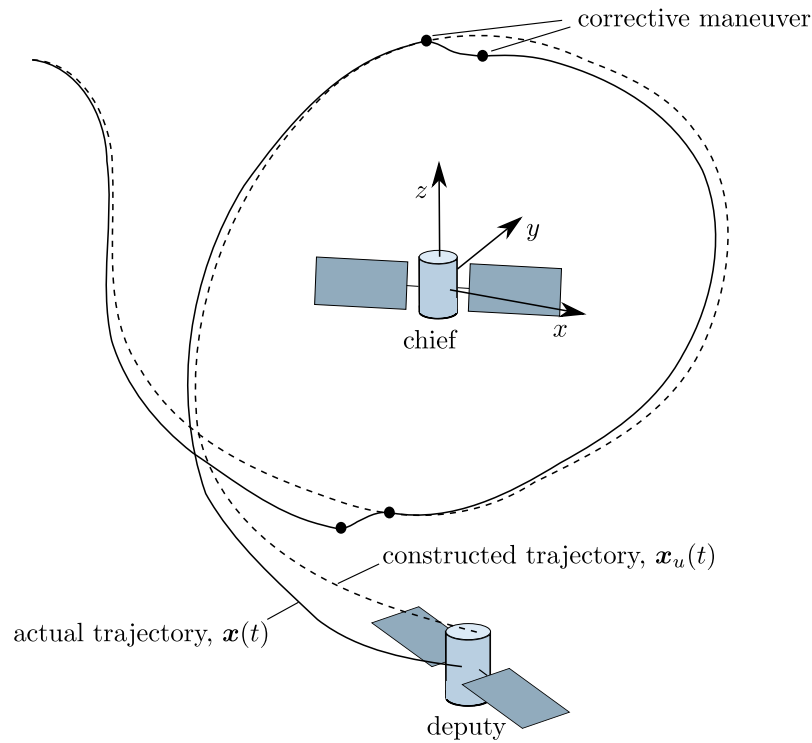


Figure 1: Relative Motion Guidance via Mode Targeting, Conceptual Figure

The execution of mode targeting in a formation flying context is depicted in Figure 1. The design trajectory x_u is constructed in advance, and the spacecraft follows it by executing small corrective maneuvers as necessary. The development of the underlying theory for such a guidance and control strategy is the primary goal of this paper.

Perturbed Orbits and Linearized Relative Motion Dynamics

The arguments in this paper assume spacecraft operating in sufficiently close proximity that non-linear effects are negligible. This would be highly applicable to fractionated space systems, ren-

dezyous and docking, and satellite servicing applications. For close-proximity relative motion in local rectilinear coordinates or orbit element differences, the linearized dynamics are of the form $\dot{\mathbf{x}} = [A(t)]\mathbf{x}$. It can be shown that $[A(t)] \approx [A(t+T)]$ if the chief spacecraft orbit is slowly varying or quasi-periodic such that there exists a *quasi-period* T for which the position and velocity are almost periodic, $\mathbf{r}(t) \approx \mathbf{r}(t+T)$, $\mathbf{v}(t) \approx \mathbf{v}(t+T)$, and furthermore $\frac{\partial \dot{\mathbf{r}}(t)}{\partial \mathbf{r}} \approx \frac{\partial \dot{\mathbf{r}}(t+T)}{\partial \mathbf{r}}$. This regularity is a desirable characteristic for spacecraft orbits in highly perturbed environments, and the resulting almost-periodicity of $[A(t)]$ also enables the analytic developments in this paper.

Instead of parameterizing the relative motion in coordinates along the radial, normal, and transverse directions $\hat{\mathbf{e}}_r = \mathbf{r}/r$, $\hat{\mathbf{e}}_n = \mathbf{h}/h$, $\hat{\mathbf{e}}_t = -\hat{\mathbf{e}}_r \times \hat{\mathbf{e}}_n$, orbit element differences are used. The quasi-nonsingular (QNS) elements linearize better than local rectilinear coordinate descriptions, without suffering the weakness for near-circular orbits inherent to the classical orbit elements.²⁴ They are given by $\boldsymbol{\alpha} = (a, \theta, i, q_1, q_2, \Omega)^\top$ where a is the semimajor axis, $\theta = \omega + f$ is the argument of latitude, i is inclination, $q_1 = e \cos \omega$ and $q_2 = e \sin \omega$ are defined in terms of the eccentricity e and argument of periapsis ω , and Ω is the right ascension of the ascending node (R.A.A.N.). Their differential equations are given below, where $r = p/(1 + q_1 \cos \theta + q_2 \sin \theta)$, $p = a(1 - q_1^2 - q_2^2)$, and $h = \sqrt{\mu p}$, and the disturbance acceleration is resolved as $\mathbf{a}_P = a_r \hat{\mathbf{e}}_r + a_t \hat{\mathbf{e}}_t + a_n \hat{\mathbf{e}}_n$:

$$\frac{da}{dt} = \frac{2a^2}{h} \left((q_1 \sin \theta - q_2 \cos \theta) a_r + \frac{p}{r} a_t \right) \quad (1a)$$

$$\frac{d\theta}{dt} = \frac{h}{r^2} - \frac{r \sin \theta \cos i}{h \sin i} a_n \quad (1b)$$

$$\frac{di}{dt} = \frac{r \cos \theta}{h} a_n \quad (1c)$$

$$\frac{dq_1}{dt} = \frac{p \sin \theta}{h} a_r + \frac{(p+r) \cos \theta + r q_1}{h} a_t + \frac{r q_2 \sin \theta}{h \tan i} a_n \quad (1d)$$

$$\frac{dq_2}{dt} = -\frac{p \cos \theta}{h} a_r + \frac{(p+r) \sin \theta + r q_2}{h} a_t - \frac{r q_1 \sin \theta}{h \tan i} a_n \quad (1e)$$

$$\frac{d\Omega}{dt} = \frac{r \sin \theta}{h \sin i} a_n \quad (1f)$$

The differential equations for orbit element differences are obtained by linearizing Eq. (1) about the chief orbit as $\delta \boldsymbol{\alpha} = \left. \frac{d\boldsymbol{\alpha}}{d\boldsymbol{\alpha}} \right|_c \delta \boldsymbol{\alpha} = [A_{\boldsymbol{\alpha}}(t)] \delta \boldsymbol{\alpha}$, where $\delta \boldsymbol{\alpha} = (\delta a, \delta \theta, \delta i, \delta q_1, \delta q_2, \delta \Omega)^\top$, and the first row of $[A_{\boldsymbol{\alpha}}(t)]$ is given below:

$$A_{11} = \frac{3a}{h} (a_t + (q_1 a_t - q_2 a_r) \cos \theta + (q_1 a_r + q_2 a_t) \sin \theta) + \frac{2a^2}{h} \left((q_1 \sin \theta - q_2 \cos \theta) \frac{da_r}{da} + \frac{p}{r} \frac{da_t}{da} \right) \quad (2a)$$

$$A_{12} = \frac{2a^2}{h} \left((q_1 a_r + q_2 a_t) \cos \theta + (q_2 a_r - q_1 a_t) \sin \theta \right) + \frac{2a^2}{h} \left((q_1 \sin \theta - q_2 \cos \theta) \frac{da_r}{d\theta} + \frac{p}{r} \frac{da_t}{d\theta} \right) \quad (2b)$$

$$A_{13} = \frac{2a^2}{h} \left((q_1 \sin \theta - q_2 \cos \theta) \frac{da_r}{di} + \frac{p}{r} \frac{da_t}{di} \right) \quad (2c)$$

$$A_{14} = \frac{2a^3 \mu}{h^3} (q_1 a_t + (a_t - q_1 q_2 a_r - q_2^2 a_t) \cos \theta + (a_r + q_1 q_2 a_t - q_2^2 a_r) \sin \theta) + \frac{2a^2}{h} \left((q_1 \sin \theta - q_2 \cos \theta) \frac{da_r}{dq_1} + \frac{p}{r} \frac{da_t}{dq_1} \right) \quad (2d)$$

$$A_{15} = \frac{2a^3\mu}{h^3} (q_2 a_t + ((q_1^2 - 1)a_r + q_1 q_2 a_t) \cos \theta + (a_t + q_1 q_2 a_r - q_1^2 a_t) \sin \theta) + \frac{2a^2}{h} ((q_1 \sin \theta - q_2 \cos \theta) \frac{da_r}{dq_2} + \frac{p}{r} \frac{da_t}{dq_2}) \quad (2e)$$

$$A_{16} = \frac{2a^2}{h} ((q_1 \sin \theta - q_2 \cos \theta) \frac{da_r}{d\Omega} + \frac{p}{r} \frac{da_t}{d\Omega}) \quad (2f)$$

There are too many terms to show all other components here, but they are straightforward to obtain. These equations were adapted to write a generalized linearization toolbox valid for any perturbed orbit problem, which was used to perform the necessary computations for this paper. The nonlinear mapping between orbit element differences and the local vertical-local horizontal (LVLH) frame relative state is achieved by adding the element differences to the chief elements to obtain the deputy orbit elements, then the chief and deputy elements are mapped to inertial coordinates, then the chief state is subtracted from the deputy and the state differences are resolved in the LVLH frame. There also exists a linearized mapping between the local coordinate description and the QNS element differences, reproduced here:¹

$$x = \frac{r}{a} \delta a + \frac{V_r}{V_t} r \delta \theta - \frac{r}{p} (2a q_1 + r \cos \theta) \delta q_1 - \frac{r}{p} (2a q_2 + r \sin \theta) \delta q_2 \quad (3a)$$

$$y = r(\delta \theta + \cos i \delta \Omega) \quad (3b)$$

$$z = r(\sin \theta \delta i - \cos \theta \sin i \delta \Omega) \quad (3c)$$

$$\dot{x} = -\frac{V_r}{2a} \delta a + \left(\frac{1}{r} - \frac{1}{p} \right) h \delta \theta + (V_r a q_1 + h \sin \theta) \frac{\delta q_1}{p} + (V_r a q_2 - h \cos \theta) \frac{\delta q_2}{p} \quad (3d)$$

$$\dot{y} = -\frac{3V_t}{2a} \delta a - V_r \delta \theta + (3V_t a q_1 + 2h \cos \theta) \frac{\delta q_1}{p} + (3V_t a q_2 + 2h \sin \theta) \frac{\delta q_2}{p} + V_r \cos i \delta \Omega \quad (3e)$$

$$\dot{z} = (V_t \cos \theta + V_r \sin \theta) \delta i + (V_t \sin \theta - V_r \cos \theta) \sin i \delta \Omega \quad (3f)$$

where V_r and V_t are given below. Note that the given mapping to velocity components does not account for the effects of perturbations.¹⁵

$$V_r = \frac{h}{p} (q_1 \sin \theta - q_2 \cos \theta) \quad (4a)$$

$$V_t = \frac{h}{p} (1 + q_1 \cos \theta + q_2 \sin \theta) \quad (4b)$$

Almost-Periodic Linear Systems

Consider a linear time-varying system $\dot{\mathbf{x}} = [A(t)]\mathbf{x}$, for which $[A(t)] \approx [A(t+T)]$ but a perturbing term $[\delta A(t)]$ stops the plant matrix from being exactly periodic:

$$\dot{\mathbf{x}} = ([\bar{A}(t)] + [\delta A(t)]) \mathbf{x} \equiv [A(t)]\mathbf{x} \quad (5)$$

In this paper, Eq. (5) represents the linearized dynamics of relative motion about an orbiter in a perturbed environment, in either LVLH frame coordinates or differential QNS elements. Note that in this discussion, the term $[\delta A(t)]$ represents the known non-periodic data in the plant matrix, but the influence of dynamic uncertainty due to low-fidelity modeling or navigational errors in the chief orbit can additionally be incorporated into this term for other analyses.

Let $\mathbf{x}_u(t)$ be the solution to the following uncorrected dynamics for which the plant matrix is exactly periodic:

$$\dot{\mathbf{x}}_u = [\bar{A}(t)]\mathbf{x}_u \quad (6)$$

For this system, the constant matrix $[\bar{\Phi}(t_0 + T, t_0)]$ is the monodromy matrix, with $[\bar{\Phi}(t, t_0)]$ being the solution of the following differential equation for the state transition matrix (STM) of \mathbf{x}_u :

$$\dot{[\bar{\Phi}(t, t_0)]} = [\bar{A}(t)][\bar{\Phi}(t, t_0)] \quad (7)$$

with the initial condition $[\bar{\Phi}(t_0, t_0)] = [I]$ Note the following transformation of the monodromy matrix due to a shift of the epoch time from t_0 to t_c :

$$[\bar{\Phi}(t_c + T, t_c)] = [\bar{\Phi}(t_c, t_0)][\bar{\Phi}(t_0 + T, t_0)][\bar{\Phi}(t_c, t_0)]^{-1} \quad (8)$$

There exists a T -periodic coordinate transformation $\mathbf{x}_u = [P(t)]\mathbf{z}_u$, with $[P(t)]$ given below:

$$[P(t)] = [\bar{\Phi}(t, t_0)]e^{-[\bar{\Lambda}](t-t_0)} \quad (9)$$

$$[P(t_0)] = [P(t_0 + T)] = [I] \quad (10)$$

Furthermore, by differentiating $\mathbf{x}_u = [P(t)]\mathbf{z}_u$ and substituting Eq. (6), it can be shown that the dynamics of \mathbf{z}_u obey the following equation with a *constant* plant matrix $[\bar{\Lambda}]$:

$$\dot{\mathbf{z}}_u = \left([P(t)]^{-1}[\bar{A}(t)][P(t)] - [P(t)]^{-1}[\dot{P}(t)] \right) \mathbf{z}_u = [\bar{\Lambda}]\mathbf{z}_u \quad (11)$$

Note in addition that $[\bar{\Lambda}]$ is computed directly from the monodromy matrix:

$$[\bar{\Lambda}] = \frac{1}{T} \ln([\bar{\Phi}(t_0 + T, t_0)]) \quad (12)$$

For the perturbed system given by Eq. (5), let a new corresponding system \mathbf{z} be constructed as $\mathbf{z} = [P(t)]^{-1}\mathbf{x}$ using the same T -periodic transformation $[P(t)]$ in Eq. (9). In other words, this new system will be dynamically equivalent to the system in \mathbf{x} , with the states mapped using the same periodic transformation that maps between the uncorrected systems. This is illustrated in Figure 2.

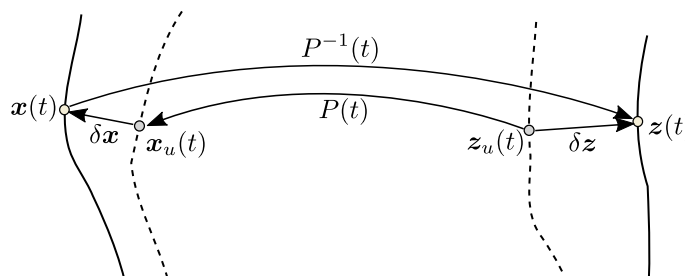


Figure 2: Transformation Between \mathbf{x} and \mathbf{z} Spaces

The dynamics of \mathbf{x} differ from those of \mathbf{x}_u by the addition of the $[\delta A(t)]$ term in the plant matrix, and the dynamics in \mathbf{z} will correspondingly differ from those of \mathbf{z}_u . The corresponding deviation in

z space dynamics must be characterized. Differentiating $x = [P(t)]z$ and substituting Eq. (5), the following equation is obtained for the dynamics in z :

$$\dot{z} = \left([P]^{-1}[\bar{A}][P] + [P]^{-1}[\delta A][P] - [P]^{-1}[\dot{P}] \right) z \quad (13)$$

Here, the term $[\bar{\Lambda}] = [P]^{-1}[\bar{A}][P] - [P]^{-1}[\dot{P}]$ is recognized, and the dynamics of z are rewritten:

$$\dot{z} = ([\bar{\Lambda}] + [\delta\Lambda(t)]) z \equiv [\Lambda(t)]z \quad (14)$$

$$[\delta\Lambda(t)] = [P(t)]^{-1}[\delta A(t)][P(t)] \quad (15)$$

Thus, on the interval $\mathcal{T} = [t_0, t_0 + T]$, the linear time-varying system in x with almost-periodic plant matrix $[A(t)] \approx [A(t + T)]$ has been transformed into a system in z with an almost constant plant matrix $[\Lambda(t)]$ subject to small oscillations $[\delta\Lambda(t)]$ about a constant $[\bar{\Lambda}]$. Eqs. (14) and (15) are of fundamental importance in this paper, as is the z space in which they operate.

Persistence and Robustness of Modes

The properties of desirable modes are now outlined. To facilitate this discussion, introduce the factorization $z = z_u + \delta z$, for which z_u obeys the following modal decomposition:

$$z_u = \sum_{i=1}^k c_i \nu_i e^{\lambda_i(t-t_0)} \quad (16)$$

Here ν_i is the i th eigenvector of $[\bar{\Lambda}]$. It is also possible to modally decompose the motion in x_u due to the existence of the transformation $x_u(t) = [P(t)]z_u(t)$. Let z be initialized in a single mode, such that $\delta z(t_0) = \mathbf{0}$, and then evolve subject to the full plant matrix via Eq. (14):

$$z_l = z_{u,l} + \delta z = c_l \nu_l e^{\lambda_l(t-t_0)} + \delta z \quad (17)$$

For simplicity, the mode is assumed to consist of a single unique eigenvalue, but this analysis could be repeated with a complex-conjugate pair of eigenvalues. Substitute Eq. (17) into Eq. (14), and consider a time range $t_0 \leq t < t^*$ such that δz is small enough to neglect in comparison to z_u . In this time range, the state evolves as:

$$\dot{z}_l = \dot{z}_{u,l} + \delta \dot{z} \approx [\bar{\Lambda}]z_{u,l} + [\delta\Lambda(t)]z_{u,l} \quad (18)$$

From Eq. (18), during the time $t_0 \leq t < t^*$, the condition that the initial modal motion be closely followed by the perturbed system is that the flow of the uncorrected mode $\dot{z}_{u,l}$ dominates that of the deviation $\delta \dot{z}$, where $\|\cdot\|$ is the operator norm or 2-norm:

$$\|[\delta\Lambda(t)]\nu_l\| \ll \|\lambda_l \nu_l\| \quad (19)$$

In other words, only the sub-eigenspace of $[\bar{\Lambda}]$ that is *robust* to the small perturbations due to $[\delta\Lambda(t)]$ will be closely reflected by the true dynamics for an appreciable period of time.

Consider two intervals $\mathcal{T}_k = [t_0 + kT, t_0 + (k+1)T]$ and $\mathcal{T}_{k+1} = [t_0 + (k+1)T, t_0 + (k+2)T]$, on which the matrices $[\bar{\Lambda}_k]$ and $[\bar{\Lambda}_{k+1}]$ are computed from the monodromy matrices associated with the periodic parts of the plant matrix on the two intervals, themselves obtained via Eq. (7):

$$[\bar{\Lambda}_k] = \frac{1}{T} \ln([\bar{\Phi}(t_0 + (k+1)T, t_0 + kT)]) \quad (20)$$

$$[\bar{\Lambda}_{k+1}] = \frac{1}{T} \ln([\bar{\Phi}(t_0 + (k+2)T, t_0 + (k+1)T)]) \quad (21)$$

Let $[\Delta\bar{\Lambda}_{k+1}] = [\bar{\Lambda}_{k+1}] - [\bar{\Lambda}_k]$. It can be said that the i th mode is *persistent* in the transition from interval \mathcal{T}_k to \mathcal{T}_{k+1} so long as the changes in the eigenvalue are small, $|\Delta\lambda_i| \ll |\lambda_i|$, and the changes in the eigenvector are small.

The desirable modes for mode-targeting are thus those which satisfy two criteria: (1) robustness, meaning that any disturbances $[\delta\Lambda(t)]$ have only secondary effects, and (2) persistence, meaning that they change only slightly with each interval. Most importantly, these two properties are expected to go hand-in-hand, because they both are indicators of the robustness of a given eigenvalue and eigenvector to arbitrary small matrix perturbations. Thus, modes that are persistent over multiple intervals should also generally be robust. It is this fact that motivates the developments in this paper.

Dynamics of the Deviation

Factoring Eq. (14) into the uncorrected component and the deviation, the following is obtained:

$$(\dot{z}_u + \delta\dot{z}) = ([\bar{\Lambda}] + [\delta\Lambda(t)])(z_u + \delta z) \quad (22)$$

It has already been established that for initialization in an appropriately chosen robust and persistent mode (or similarly, a combination of such modes), $z(t) \approx z_u(t)$ for some time range $t_0 \leq t < t^*$. On this time range, an approximate expression for the deviation $\delta z(t)$ is sought. This can be obtained with a straightforward perturbation expansion, by introducing the scalings $[\Lambda(t)] = [\Lambda_0] + \epsilon[\Lambda_1]$ and $z = z_0 + \epsilon z_1$, where the zeroth-order terms are $[\Lambda_0] = [\bar{\Lambda}]$ and $z_0 = z_u$, and the first-order terms are $\epsilon[\Lambda_1] = [\delta\Lambda]$ and $\epsilon z_1 = \delta z$. Substituting these expansions into Eq. (22) and isolating the $\mathcal{O}(\epsilon^0)$ and $\mathcal{O}(\epsilon^1)$ components, the following two equations are obtained:

$$\dot{z}_0 = [\Lambda_0]z_0 \quad (23)$$

$$\dot{z}_1 = [\Lambda_0]z_1 + [\Lambda_1]z_0 \quad (24)$$

Multiplying Eq. (24) by ϵ , substituting in $z_0 = z_u(t)$ and the other scaling definitions, and allowing for a small nonzero initial condition on the deviation $\delta z(t_0) = \Delta z$, the solution to the approximate dynamics of the deviation are given below, where $[\bar{\Phi}_z(t, \tau)] = \exp([\bar{\Lambda}](t - \tau))$:

$$\delta z(t) \approx \int_{t_0}^t [\bar{\Phi}_z(t, \tau)][\delta\Lambda(\tau)][\bar{\Phi}_z(\tau, t_0)]d\tau \cdot z_u(t_0) + [\bar{\Phi}_z(t, t_0)]\Delta z \quad (25)$$

This equation is valid so long as the deviation remains sufficiently small that the deriving assumptions are not violated. The term Δz represents a small targeting error, $z(t_0) - z_u(t_0)$. The derivation of Eq. (25) concludes the analytic prerequisites for discussing a mode targeting technique.

GUIDANCE AND CONTROL IMPLEMENTATION

General Mode Targeting Procedure

A preliminary mode-targeting control strategy can be implemented via the following procedure:

1. Using the highest-accuracy dynamic model available, compute plant matrix for the relative motion linearization $\dot{x} = [A(t)]x$, with $[A(t)] \approx [A(t+T)]$, and timespan of interest broken into adjacent intervals $\mathcal{T}_k = [t_0 + kT, t_0 + (k+1)T]$. Compute $[\bar{A}_k(t)]$ on each interval by Fourier fit of $[A(t)]$.

2. Compute the state transition matrix associated with the periodic component of the plant matrix, $[\overline{\Phi}_k(t, t_0)] \equiv [\overline{\Phi}(t, t_0 + kT)]$ and the z_u space plant matrix $[\overline{\Lambda}_k]$ on each interval. Also compute $[P(t)]$ for each interval.
3. From the eigenspace of each $[\overline{\Lambda}_k]$, identify the persistent modes, which are modes that change only slightly across intervals. These modes form the basis of available relative motion that can be accomplished despite the presence of non-periodic components in the plant matrix and mild navigational and dynamic uncertainty. Recall that this is due to the expectation that persistent modes should also be robust to small perturbations.
4. Design the desired behavior $x_u(t) = [P(t)]z_u(t)$ as a superposition of the available modes on each interval, with the end conditions in one interval patched to the closest obtainable state vector in the following interval. Note that for modes that change only slightly between two intervals \mathcal{T}_k and \mathcal{T}_{k+1} , the modes from interval \mathcal{T}_k can be used in the design of x_u in interval \mathcal{T}_{k+1} , and possibly beyond. In other words, maneuvers between intervals need not always be used for developing the design trajectory, if the modes change sufficiently slowly.
5. In addition to the possible need of small maneuvers in the transitions between intervals, the accumulation of dynamic and navigational errors establishes a need for small corrective maneuvers to drive the true motion $x(t)$ back to the desired motion $x_u(t)$. For analytic rigor, it is necessary to establish a suitable corrective maneuver timescale Δt for the spacecraft to re-target the desired trajectory. One approach for obtaining this value of Δt is discussed.
6. Design a control strategy to perform the necessary corrective maneuvers, driving $x(t)$ to $x_u(t)$ in short control arcs every Δt time units. A simple approach is described in this paper.

Each of the steps in this procedure are discussed further as needed in the remainder of the paper.

Estimating Corrective Maneuver Frequency

One can conservatively estimate an appropriate time between corrective maneuvers Δt by estimating an upper bound on the time for the deviation to achieve a magnitude that is some critical fraction α_1 of the initial state norm. In other words, a Δt is sought such that $\|\delta z(\Delta t)\| < \alpha_1 \|z_u(0)\|$, where $\alpha_1 \ll 1$. Using Eq. (25) and writing $t_0 \equiv 0$ for notational convenience:

$$\|\delta z(\Delta t)\| = \left\| \int_0^{\Delta t} [\overline{\Phi}_z(\Delta t, \tau)] [\delta \Lambda(\tau)] [\overline{\Phi}_z(\tau, 0)] d\tau \cdot z_u(0) + [\overline{\Phi}_z(\Delta t, 0)] \Delta z \right\| \quad (26)$$

Using the sub-multiplicative and triangle inequality properties of the 2-norm, and the integral inequality $\left\| \int_a^b [X(\varphi)] d\varphi \right\| \leq \int_a^b \|X(\varphi)\| d\varphi$:

$$\|\delta z(\Delta t)\| \leq \int_0^{\Delta t} \|\overline{\Phi}_z(\Delta t, \tau)\| \|\delta \Lambda(\tau)\| \|\overline{\Phi}_z(\tau, 0)\| d\tau \|z_u(0)\| + \|\overline{\Phi}_z(\Delta t, 0)\| \|\Delta z\| < \alpha_1 \|z_u(0)\| \quad (27)$$

Limiting the scale of a term larger than $\|\delta z(\Delta t)\|$ will also limit the scale of $\|\delta z(\Delta t)\|$, so the middle term in the inequality Eq. (27) is the focus for subsequent manipulations.

Noting that $[\overline{\Phi}_z(\Delta t, \tau)] = \exp([\overline{\Lambda}](\Delta t - \tau))$, an upper bound of the matrix exponential is needed. The general matrix exponential $\exp([F]t)$ for arbitrary $[F]$ is upper-bounded by the following:²²

$$\|\exp([F]t)\| \leq \sqrt{c(r)} \exp(\theta(r)t), \quad t \geq 0 \quad (28)$$

where r is a number satisfying $r > r_{\max}(F)$, with $r_{\max}(F) := \max\{\text{Re}(\lambda) : \lambda \in \lambda(F)\}$, such that the eigenvalues of the new matrix $F(r) = [F] - r[I]$ lie strictly in the left-half plane. The term $c(r)$ is to be defined, and $\theta(r) = r - \kappa(r)$, with $\kappa(r) = 1/(2\|Z(r)\|)$. The term $[Z(r)]$ is a positive-definite Hermitian matrix solving the algebraic Lyapunov equation:

$$[Z(r)][F(r)] + [F^*(r)][Z(r)] = -I \quad (29)$$

where $*$ denotes the conjugate transpose. Now the definition of $c(r)$ may be given:

$$c(r) = \min \{ \|Z(r)^{-1}\| \|Z(r)\|, c(a, b) \} \quad (30)$$

$$c(a, b) = \left(\frac{1+b}{1+ab} \right)^{1+1/b} \quad (31)$$

$$a = \kappa(r)/|h_{\min} - r|, \quad b = (h_{\max} - r)/\kappa(r) \quad (32)$$

where h_{\min} and h_{\max} are the minimum and maximum eigenvalues respectively of the Hermitian matrix $(F + F^*)/2$. Returning to Eq. (27) and applying the new definitions:

$$\begin{aligned} \|\delta z(\Delta t)\| &\leq \int_0^{\Delta t} \|\bar{\Phi}_z(\Delta t, \tau)\| \|\delta \Lambda(\tau)\| \|\bar{\Phi}_z(\tau, 0)\| d\tau \|z_u(0)\| + \|\bar{\Phi}_z(\Delta t, 0)\| \|\Delta z\| \\ &< \left(\int_0^{\Delta t} \sqrt{c(r_\Lambda)} \exp(\theta(r_\Lambda)(\Delta t - \tau)) U \sqrt{c(r_\Lambda)} \exp(\theta(r_\Lambda)\tau) d\tau \|z_u(0)\| \right. \\ &\quad \left. + \sqrt{c(r_\Lambda)} \exp(\theta(r_\Lambda)\Delta t) \alpha_2 \|z_u(0)\| \right) \\ &< \alpha_1 \|z_u(0)\| \end{aligned} \quad (33)$$

where $r_\Lambda > r_{\max}(\bar{\Lambda})$, and $c(r_\Lambda)$, $\theta(r_\Lambda)$ are obtained by computing $c(r)$ and $\theta(r)$ for $[\bar{\Lambda}]$ using the previously outlined procedure.²² Some new terms are also introduced in Eq. (33). The term $\alpha_2 \|z_u(0)\|$ is a reasonable worst-case estimate of the targeting error Δz at the end of the previous maneuver $t_0 \equiv 0$, and the constants α_1, α_2 must satisfy $\alpha_2 \ll \alpha_1$ by definition. This term enables the predicted maximum error of the corrective maneuver control scheme to be accounted for in the estimate for the time between control corrections, Δt . The term $U = \|\delta \Lambda^\dagger\|$ represents the norm of a worst-case $[\delta \Lambda(t)]$ yielding the largest maximum norm $\|\delta \Lambda(t)\|$ of any time t on the given interval \mathcal{T} . Thus, U is a term that accounts for worst-case expected combined effects of non-periodicity of the plant matrix, dynamical error and navigational error in the chief orbit. Note that in the context of unbounded probability distributions, a worst-case quantity would simply mean the worst possible value obtained from within some suitable limits of the distribution of all possible outcomes, such as the 3σ limits. Discussions of the computation or estimation of this term are left for future work.

Simplifying the middle term in Eq. (33) and cancelling the $\|z_u(0)\|$ terms, obtain the following:

$$\exp(\theta(r_\Lambda) \Delta t) \left(c(r_\Lambda) U \Delta t + \sqrt{c(r_\Lambda)} \alpha_2 \right) < \alpha_1 \quad (34)$$

Eq. (34) illustrates that the inequality $\alpha_1/\alpha_2 > \sqrt{c(r_\Lambda)}$ must be satisfied to obtain a physical time between corrective maneuvers $\Delta t > 0$. The post-maneuver error measure α_2 and the properties of

$[\bar{\Lambda}]$ determine the achievable deviation measure α_1 . Eq. (34) is solved to obtain the estimate of time Δt between corrective maneuvers on a given interval:

$$\Delta t < \frac{1}{\theta(r_\Lambda)} W \left(\frac{\alpha_1 \cdot \exp \left(\frac{\theta(r_\Lambda)\alpha_2}{\sqrt{c(r_\Lambda)U}} \right) \theta(r_\Lambda)}{c(r_\Lambda)U} \right) - \frac{\alpha_2}{\sqrt{c(r_\Lambda)U}} \quad (35)$$

where $W(\cdot)$ denotes the Lambert W-function, and because the argument of W in Eq. (35) is positive, this expression is single-valued. Eq. (35) concisely captures the relationship between the combined effects of non-periodicity of the original plant matrix, dynamic uncertainty, and control maneuver accuracy to keep the maximum deviation from the design trajectory constrained to be less than a chosen maximum. It is particularly useful because it is not a function of the state, and only needs to be computed once per interval.

Corrective Maneuver Control Implementation

A strategy for applying small corrective maneuvers such that $\mathbf{x}(t)$ is driven back to $\mathbf{x}_u(t)$ is needed. Furthermore, it must be sufficiently accurate to satisfy the performance requirements outlined previously. For the sake of onboard implementation, it is highly desirable that any such strategy takes advantage of the fact that the needed corrections for mode targeting are always small, and should be short in duration. One approach is to use a relative motion state transition matrix (STM) to design the necessary impulsive maneuvers. To control to a future target condition $\mathbf{x} = [\Delta \mathbf{r}^\top, \Delta \mathbf{r}'^\top]^\top$ at time t from a maneuver initial condition $\mathbf{x}_m = [\Delta \mathbf{r}_m^\top, \Delta \mathbf{r}'_m{}^\top]^\top$ at time t_m , the following factoring of the state transition matrix is used:

$$[\Phi(t, t_m)] = \begin{bmatrix} \Phi_{rr}(t, t_m) & \Phi_{rv}(t, t_m) \\ \Phi_{vr}(t, t_m) & \Phi_{vv}(t, t_m) \end{bmatrix} \quad (36)$$

from which the final state may be expressed in terms of the state at the initial time:

$$\Delta \mathbf{r} = [\Phi_{rr}(t, t_m)]\Delta \mathbf{r}_m + [\Phi_{rv}(t, t_m)]\Delta \mathbf{r}'_m \quad (37)$$

$$\Delta \mathbf{v} = [\Phi_{vr}(t, t_m)]\Delta \mathbf{r}_m + [\Phi_{vv}(t, t_m)]\Delta \mathbf{r}'_m \quad (38)$$

Substituting the desired position $\Delta \mathbf{r}^*$ in Eq. (37), the first delta-V of δ_1 to achieve this position is isolated:

$$\Delta \mathbf{r}^* = [\Phi_{rr}(t, t_m)]\Delta \mathbf{r}_m + [\Phi_{rv}(t, t_m)] (\Delta \mathbf{r}'_m{}^- + \delta_1) \quad (39)$$

where $\Delta \mathbf{r}'_m{}^-$ is the velocity at time t_m before the first delta-V. Solving for δ_1 :

$$\delta_1 = [\Phi_{rv}(t, t_m)]^{-1} (\Delta \mathbf{r}^* - [\Phi_{rr}(t, t_m)]\Delta \mathbf{r}_m) - \Delta \mathbf{r}'_m{}^- \quad (40)$$

Similarly, from the initial conditions and the STM, the second delta-V at the end of the maneuver may be estimated in advance:

$$\delta_2 = \Delta \mathbf{r}'^* - ([\Phi_{vr}(t, t_m)]\Delta \mathbf{r}_m + [\Phi_{vv}(t, t_m)]\Delta \mathbf{r}'_m{}^+) \quad (41)$$

where $\Delta \mathbf{r}'_m{}^+ = \Delta \mathbf{r}'_m{}^- + \delta_1$. Note that for sufficiently small and short duration burns, state transition matrices for Keplerian relative motion may be used, such as the Clohessy-Wiltshire state transition matrix,¹¹ if the chief orbit is nearly circular, or the Yamanaka-Anderson state transition matrix,²⁸ if

the orbit is more eccentric. This is because over very short intervals of time, the relative motion is still well-described by the unperturbed relative motion solution.

Multiple burns over a maneuver period of duration $t - t_m$ may be necessary to achieve a desired target condition with sufficient accuracy. This is especially true if a Keplerian relative motion STM is used instead of the actual STM for the perturbed relative motion. This would be done by re-computing δ_1 and firing multiple corrections during the maneuver arc between t_m and t . Note that the final impulsive maneuver δ_2 simply corrects the relative velocity at time t .

APPLICATION TO ASTEROID ORBITER MISSIONS

The modal decomposition tools are now applied to the problem of design and control of close-proximity spacecraft relative motion around an asteroid. This is a useful problem of study because of both the growing popularity of asteroid missions and the potential for future spacecraft missions to trend more towards low-cost fractionated designs.^{2,19} In addition, there is an availability of nearby asteroids which are good targets for scientific study, yet reachable by small, low-cost spacecraft.¹³

The application in this work is the study of relative motion modes in terminator orbits about the asteroid 162173 Ryugu, a near-Earth asteroid which was the target of the recent Hayabusa2 mission. The rotating gravity field and the combined effects of solar gravity and radiation pressure make this a dynamically complex target for formation design or any other multi-spacecraft proximity operations, and the natural close-proximity spacecraft relative motion modes in this environment will be interesting to characterize. This example also helps to illustrate that the modal decomposition tools and techniques introduced in this paper can be applied even to very complex orbits.

Terminator Orbits

For this work, periodic terminator orbits computed in the Augmented Normalized Hill Three-Body Problem (ANH3BP) serve as the nominal orbit conditions for the chief orbit in the formation, but the true orbit is perturbed by the rotating irregular gravity field of the asteroid. Thus, the nominal orbit design is periodic, but the actual orbits will be generally quasi-periodic. Under the influence of perturbations, regular long-term stable motion can still be found in the vicinity of nominal periodic terminator orbits.⁶

Past studies have demonstrated that so long as the semimajor axis is above a 1.5 resonance radii limit and below a corresponding upper limit characterized by the third-body and SRP perturbations, the orbit will be more likely to persist for long time spans:^{17,25,26}

$$\frac{3}{2} \left(\frac{T_r^2 \mu}{4\pi^2} \right)^{1/3} < a < \frac{1}{4} \sqrt{\frac{\mu B}{G_1}} d \quad (42)$$

Here T_r is the rotation period of the asteroid, μ is its gravitational parameter, B is the spacecraft mass-to-area ratio in kg/m^2 , $G_1 \approx 10^8 \text{kg} \cdot \text{km}^3/\text{s}^2\text{m}^2$ is the solar constant, and d is the distance from the asteroid to the sun in km. Note also that the semimajor axis can be expressed as a function of the parameter $\Gamma = c/n$, where c is the rotation rate of the asteroid and n is the mean motion of the spacecraft orbit:

$$a = \Gamma^{2/3} \left(\frac{T_r^2 \mu}{4\pi^2} \right)^{1/3} \quad (43)$$

thus the rotation rate ratio inequality to guard against the effects of the rotating gravity field is $\Gamma > (3/2)^{3/2} \approx 1.8$. With the nominal orbit designed as a periodic orbit with size satisfying the

constraints of Eq. (42), the effect of the perturbations can be minimized to some degree. Furthermore, a useful degree of regularity can be introduced to the orbit by choosing the value of Γ to be rational and of the following form:

$$\Gamma^*(j, k, l) = \frac{kl + j}{k} \quad (44)$$

where j , k , and l are integers chosen such that Γ is greater than the lower limit, $j \leq k$. This choice of Γ results in $l + j/k$ rotations of the asteroid with after each spacecraft orbit period T_s . Thus, the sun-orbiter-asteroid geometry for time t and time $t + T_s$ will be the same, except the longitude of the asteroid will have advanced by $2\pi j/k$. This regularity helps to ensure that the plant matrix for relative motion will obey $[A(t)] \approx [A(t + T)]$ so that the relative motion modes can be easily characterized, and in this case $T = T_s k$. It could also be potentially useful for scientific studies by providing regularly reproducible and highly predictable lighting conditions.

The ANH3BP describes motion in the vicinity of a sun-orbiting asteroid, and the dynamics are given by the following dimensionless equations of motion for a circular asteroid heliocentric orbit:⁷

$$\mathbf{r}'' + \hat{\mathbf{z}} \times \mathbf{r}' + (\hat{\mathbf{z}} \cdot \mathbf{r}) \hat{\mathbf{z}} = \frac{\partial U}{\partial \mathbf{r}} \quad (45)$$

$$U(\mathbf{r}) = \frac{1}{\|\mathbf{r}\|} + \beta \hat{\mathbf{d}} \cdot \mathbf{r} + \frac{3}{2} (\hat{\mathbf{d}} \cdot \mathbf{r})^2 \quad (46)$$

where $\hat{\mathbf{d}}$ is the unit vector pointing from the sun to the asteroid and β is the non-dimensional SRP acceleration in terms of the solar constant G_1 , mass-to-area ratio B , solar gravitational parameter μ_s , and asteroid gravitational parameter μ :

$$\beta = \frac{G_1}{B \mu_s^{2/3} \mu^{1/3}} \quad (47)$$

Note that β is the only parameter of interest in the non-dimensional problem. The terms \mathbf{r} and \mathbf{r}' are the dimensionless orbiter position and velocity about the asteroid in the rotating asteroid-fixed Hill frame, related to the dimensionalized position \mathbf{R} and velocity $\dot{\mathbf{R}}$ in the rotating frame by the expressions given below:

$$\mathbf{r} = \frac{1}{\epsilon d} \mathbf{R} \quad (48)$$

$$\mathbf{r}' = \frac{1}{\epsilon d \Omega_n} \dot{\mathbf{R}} \quad (49)$$

where d is the sun-asteroid distance, $\epsilon = (\mu/\mu_s)^{1/3}$, and $\Omega_n = \sqrt{\mu_s/d^3}$. These equations are adapted from more general eccentric orbit equations, and Eqs. (45) and (49) change for the general elliptic case.²⁶ Note that Eq. (45) admits a Jacobi integral, which is conserved for any orbit, and given below in terms of the potential $U(\mathbf{r})$ and $v = \|\mathbf{r}'\|$ and $z = \mathbf{r} \cdot \hat{\mathbf{z}}$

$$C_J = \frac{1}{2} (v^2 + z^2) - U(\mathbf{r}) \quad (50)$$

Periodic orbits are found using a multiple-shooting predictor-corrector algorithm, which breaks the trajectory into q segments with initial states \mathbf{X}_i for $i = 1, \dots, q$, and these states are combined with the segment time duration $t_{\text{seg}} = T_s/q$ into the state vector \mathbf{Z} :⁷

$$\mathbf{Z} = \left[\mathbf{X}_1^\top, \mathbf{X}_2^\top, \dots, \mathbf{X}_q^\top, t_{\text{seg}} \right]^\top \quad (51)$$

By driving the following vector $\mathbf{G}(\mathbf{Z})$ to zero, the algorithm drives an initial guess of the orbit towards a nearby periodic orbit, if it exists. The zero constraint on the three select components of \mathbf{X}_1 and the Jacobi integral value constraint restrict the search space for the periodic orbit:

$$\mathbf{G}(\mathbf{Z}) = \left[\mathbf{X}_2^\top - \mathbf{F}_{t_{\text{seg}}}^\top(\mathbf{X}_1), \mathbf{X}_3^\top - \mathbf{F}_{t_{\text{seg}}}^\top(\mathbf{X}_2), \dots, \mathbf{X}_q^\top - \mathbf{F}_{t_{\text{seg}}}^\top(\mathbf{X}_{q-1}), \right. \\ \left. \mathbf{X}_1^\top - \mathbf{F}_{t_{\text{seg}}}^\top(\mathbf{X}_q), y_1, \dot{x}_1, \dot{z}_1, C(\mathbf{X}_1) - C_0 \right]^\top = \mathbf{0} \quad (52)$$

The resulting correction to \mathbf{Z} is of the form $\mathbf{Z}_{k+1} = \mathbf{Z}_k - \delta\mathbf{Z}$, with $\delta\mathbf{Z}$ given as:

$$\delta\mathbf{Z} = \gamma \left([\mathbf{H}]^\top [\mathbf{H}] \right)^{-1} [\mathbf{H}]^\top \mathbf{G}(\mathbf{Z}) \quad (53)$$

where $[\mathbf{H}] = \partial\mathbf{G}/\partial\mathbf{Z}|_{\mathbf{Z}_k}$ and $\gamma \leq 1$ is a variable step size for better convergence of the algorithm.

In order to determine the family of periodic terminator orbits applicable to this paper, the value of β for this problem must be determined, and the size of appropriate admissible dimensionless orbits must also be obtained. The former problem is a straightforward computation given B, μ, μ_s , and the latter can be solved by choosing orbits that ensure that the previously mentioned inequality $\Gamma > (3/2)^{3/2}$ is satisfied. It turns out that using $z(0) = \tilde{a}, \dot{y}(0) = 1/\tilde{a}^{1/2}$ as an initial guess tends to yield periodic terminator orbits with dimensionless periods very close to $\tilde{T} = 2\pi\tilde{a}^{3/2}$. It is thus straightforward to find the conditions for a periodic orbit with an acceptable value of dimensionless period $\tilde{T} = \Omega T_s = \Omega \Gamma T_r$, derived from a given asteroid rotation period T_r and an acceptable choice of Γ . Re-dimensionalizing the computed initial conditions will result in a satisfactory terminator orbit. Important information for this problem is summarized in Table 1, along with the semimajor axis for select values of Γ .

Table 1: Important Physical Parameters

Parameters	Values
Geometric	$d = 1.1466 \text{ AU}, B = 24.7 \text{ kg/m}^2$
Nondimensional	$\beta = 50, \Omega_n = 1.62334 \times 10^{-7}, \epsilon = 6.0873 \times 10^{-5}$
Asteroid properties ^{12, 14}	$\mu = 3 \times 10^{-8} \text{ km}^3/\text{s}^2, T_r = 7.6326 \text{ hrs}, R = 0.4484 \text{ km}$ $C_{20} = -0.0539, C_{22} = 0.0027, C_{30} = 0.00307, C_{40} = 0.04209$
Asteroid orbit	$a = 1.1896 \text{ AU}, e = 0.1902, \Omega = 251.589^\circ, i = 5.884^\circ,$ $\omega = 211.436^\circ, f_0 = \pi/2$
Asteroid orientation ¹⁴	$\lambda_p = 179.3^\circ, \beta_p = -87.44^\circ, \phi_p = 153.9^\circ, \nu_p = 171.64^\circ, \psi_{p,0} = 0^\circ$
Semimajor axis, $a(\Gamma)$	$a(2) = 1.319, a(5/2) = 1.531, a(3) = 1.728, a(7/2) = 1.916 \text{ km}$ $a(4) = 2.094, a(6) = 2.744 \text{ km}$

In Table 1, note that d is the distance from the sun to the asteroid at the beginning of the simulation, R denotes the maximum radius, and the C_{ij} terms are the low degree and order gravitational harmonics generated from the Ryugu shape model using a constant-density assumption.¹² The rotation period of Ryugu is $T_r = 7.6326 \text{ hrs}$, so admissible semimajor axes fall in the range $1.246 < a < 3.691 \text{ km}$, and the given semimajor axis values all fall within this range. In the provided orientation data, the terms λ_p and β_p are the ecliptic longitude and latitude to the spin axis. These yield an obliquity of the spin axis of 171.64° , so Ryugu rotates retrograde with respect to its

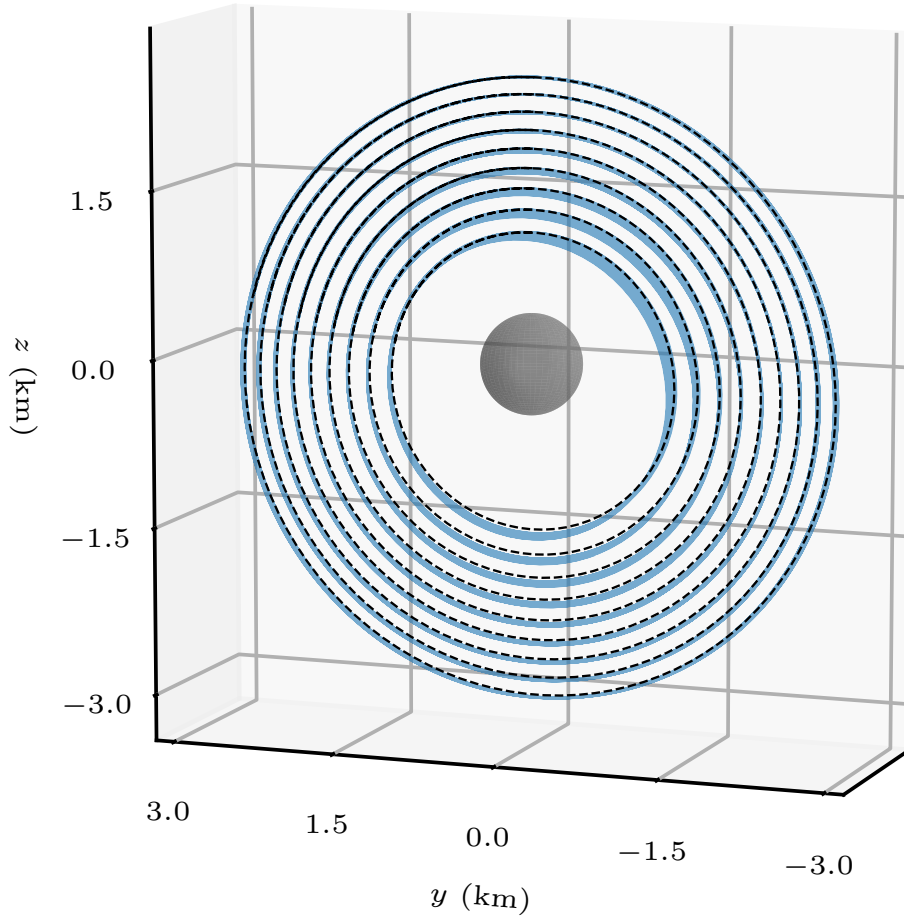


Figure 3: Nominal and Perturbed Terminator Orbits at Ryugu

orbit. The parameters $\phi_p, \nu_p, \psi_{p,0}$ are derived sequential Euler angles for the 3-1-3 rotation from the asteroid orbit perifocal frame to the asteroid body frame parameterized by the principal axes. Note $\psi_p(t) = \psi_{p,0} + ct$ for uniform rotation.

While the gravitational coefficients given in Table 1 are sufficient to capture the dominant dynamics, the effects of higher-order gravitational perturbations are added in the simulations by artificially generating higher order C_{lm} coefficients for even $l \geq m$ from C_{20} and C_{22} using the following generating function valid for constant-density ellipsoidal bodies:^{5,8}

$$C_{lm} = 3\chi (2 - \delta_{0m}) \frac{5^{\frac{l}{2}} (\frac{l}{2})! (l-m)!}{(l+3)(l+1)!} \sum_{i=0}^{\text{int}(\frac{l-m}{4})} \frac{C_{20}^{\frac{l}{2} - (\frac{m}{2} + 2i)} C_{22}^{\frac{m}{2} + 2i}}{(\frac{l}{2} - \frac{m}{2} - 2i)! (\frac{m}{2} + i)!} \quad (54)$$

where χ is a multiplier introduced because the value of C_{40} from Table 1 is greater than predicted with this equation, thus $\chi = |C_{40,\text{true}}/C_{40,\text{comp}}|$. In reality, Ryugu is not a constant-density ellipsoid, so these generated coefficients won't match the true values. In future work it would be possible to obtain more accurate values for the higher-order coefficients using the Ryugu shape model data.

A subset of the family of periodic terminator orbits is computed for $\beta = 50$ and given in Figure 3. The black curves are generated by scaling the ANH3BP-predicted periodic orbit initial conditions

and propagating with only the asteroid point-mass gravity, solar gravity, and cannonball solar radiation pressure. The light blue curves are the perturbed terminator orbits, propagated for 20 orbits from the same nominal periodic orbit initial condition, but subject to the additional disturbances of a rotating 12th degree and order gravity field generated from the data in Table 1 and Eq. (54). From the figure, it is evident that the effects of the perturbations are larger for orbits closer to Ryugu. Nonetheless, these orbits are still far more regular than orbits generated by other means, such as propagation from a circular orbit initial condition in the terminator plane.

Mode-Computing Algorithm Validation and Semi-Analytic Developments

As a preliminary test of the code for computing the modal decomposition code in orbit element differences, a 1.531 km orbit about Ryugu is tested with only the J_2 perturbation. For the J_2 -only problem, the code predicts a relative motion mode with a zero eigenvalue corresponding to relative motion consisting only of the z_6 coordinate, and the bottom row of $[P(t)]$ is zero except for the last element, thus $\delta\Omega = z_6$. In other words, the modal decomposition has successfully identified that relative motion in orbit element space consisting only of a RAAN difference will not drift or change at all over time due to the axial symmetry in the dynamics.

In addition, note that while the computed $[P(t)]$ matrix has a highly complex form when \mathbf{x} is in local rectilinear coordinates, that is not the case when \mathbf{x} is in QNS element differences. In this case, numerical results show that the transformation is near-identity, Eq. (55), with two larger time-varying elements producing the mapping $z_2 \approx \delta\theta - \xi_1(f)\delta q_1 - \xi_2(f)\delta q_2$, and smaller time-varying oscillations about zero in nearly all components, represented by $[P_\epsilon(t)]$.

$$\begin{pmatrix} \delta a \\ \delta\theta \\ \delta i \\ \delta q_1 \\ \delta q_2 \\ \delta\Omega \end{pmatrix} = \begin{bmatrix} 1 & 0 & 0 & 0 & 0 & 0 \\ 0 & 1 & 0 & \xi_1(t) & \xi_2(t) & 0 \\ 0 & 0 & 1 & 0 & 0 & 0 \\ 0 & 0 & 0 & 1 & 0 & 0 \\ 0 & 0 & 0 & 0 & 1 & 0 \\ 0 & 0 & 0 & 0 & 0 & 1 \end{bmatrix} \begin{pmatrix} z_1 \\ z_2 \\ z_3 \\ z_4 \\ z_5 \\ z_6 \end{pmatrix} + [P_\epsilon(t)]\mathbf{z}_u \quad (55)$$

This provides some insight in the modal coordinates when the relative motion modes are computed from the QNS element differences. By this coordinate similarity, it is useful to think of the \mathbf{z}_u space as one that is much like orbit element differences.

Applying the Mode-Computing Algorithm to Ryugu Terminator Orbits

The modal decompositions obtained for the perturbed terminator orbit with $\Gamma = 3$ are discussed next. The quasi-period for the perturbed orbit is determined as the time between chief orbit crossings of the plane $y = 0$ in Figure 3. The result is approximately 1% greater than the result predicted by the dimensionless system using $T = \tilde{T}/\Omega_n$. The eigenvalues of $[\bar{\Lambda}]$ are listed in Table 2 and plotted in Figure 4(a) for three successive intervals \mathcal{T}_0 , \mathcal{T}_1 , and \mathcal{T}_2 . Also included are the initial conditions for a slowly-changing mode on the three subsequent intervals, in QNS orbit element differences $\delta\mathbf{oe}_0 = \mathbf{z}_0 = [\delta a_0, \delta\theta_0, \delta i_0, \delta q_{1,0}, \delta q_{2,0}, \delta\Omega_0]$, with δa_0 in km and all angle differences in radians. It is worth noting that the pair of eigenvalues $\lambda_{5,6}$ closest to zero for interval \mathcal{T}_0 moved around significantly depending on the value of the quasi-period used to compute $[\bar{A}(t)]$, whereas the other four eigenvalues are comparatively unaffected by small changes to the quasi-period. The other four eigenvalues $\lambda_{1,2}$ and $\lambda_{3,4}$ also change very little between intervals, as can be seen by examining the two complex-conjugate pairs farthest from the real line. Note that the points for

these four eigenvalues on intervals 0, 1, and 2 lie almost on top of one another in Figure 4. The mode corresponding to the pair $\lambda_{1,2}$ is selected, and the corresponding motion is given in the LVLH frame for 12 orbits in Figure 4(b). This figure shows that the modal motion computed in interval \mathcal{T}_0 is *persistent* – i.e. it is highly similar to the motion computed for intervals \mathcal{T}_1 and \mathcal{T}_2 as well. Note that the original space of this mode is in z_u coordinates, computed using the methods introduced earlier in the paper, and its motion is mapped to LVLH coordinates by first using $[P(t)]$ to map to QNS element differences, followed by the approximate linear mapping to LVLH given by Eq. (3). The relative motion analysis was performed in QNS element differences, and the plots in this section are given in LVLH coordinates only as a visual aid to the reader.

Table 2: Spacecraft Relative Motion Modal Data for Terminator Orbit, $\Gamma = 3$

Parameters	Values
Interval \mathcal{T}_0 eigenvalues	$\lambda_{1,2} = 9.16 \times 10^{-8} \pm 1.58 \times 10^{-6}i$, $\lambda_{3,4} = -9.21 \times 10^{-8} \pm 1.58 \times 10^{-6}i$ $\lambda_{5,6} = 0.27 \times 10^{-8} \pm 2.02 \times 10^{-7}i$
Interval \mathcal{T}_0 mode initial conditions	$\delta\mathbf{oe}_0 = [-0.001, 0.039, 0.0007, 0.015, 0.016, -0.002]$
Interval \mathcal{T}_1 eigenvalues	$\lambda_{1,2} = 8.21 \times 10^{-8} \pm 1.57 \times 10^{-6}i$, $\lambda_{3,4} = -8.24 \times 10^{-8} \pm 1.57 \times 10^{-6}i$ $\lambda_{5,6} = 0.66 \times 10^{-8} \pm 6.69 \times 10^{-7}i$
Interval \mathcal{T}_1 mode initial conditions	$\delta\mathbf{oe}_0 = [-0.001, 0.039, -0.0004, 0.014, 0.016, -0.003]$
Interval \mathcal{T}_2 eigenvalues	$\lambda_{1,2} = 7.46 \times 10^{-8} \pm 1.56 \times 10^{-6}i$, $\lambda_{3,4} = -7.46 \times 10^{-8} \pm 1.56 \times 10^{-6}i$ $\lambda_{5,6} = 0.99 \times 10^{-8} \pm 8.18 \times 10^{-7}i$
Interval \mathcal{T}_2 mode initial conditions	$\delta\mathbf{oe}_0 = [-0.001, 0.037, -0.0017, 0.014, 0.018, -0.005]$

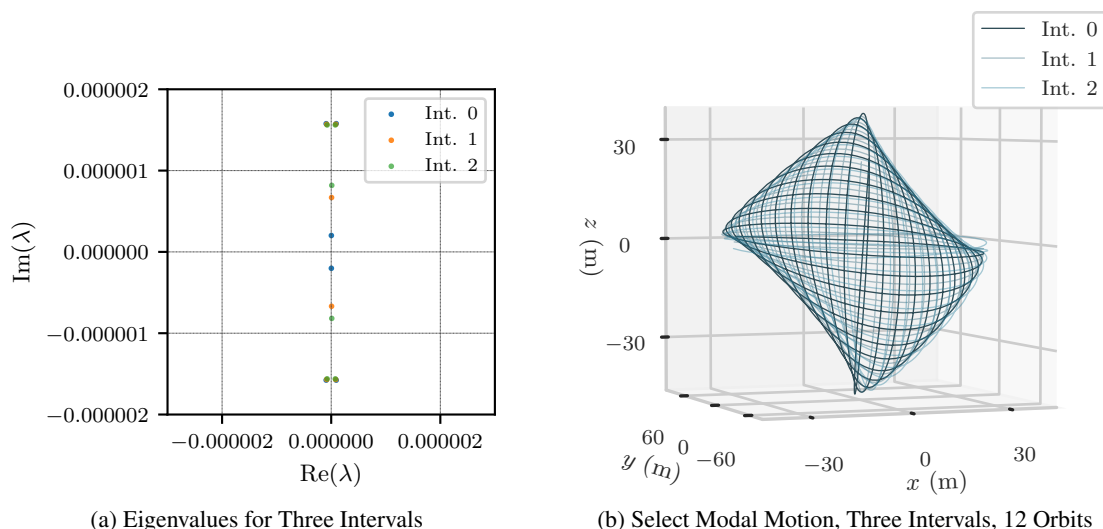


Figure 4: Modal Results for Formations in $\Gamma = 3$ Terminator Orbit

Note that the differences between $[A(t)]$ and $[\bar{A}(t)]$ are small for most components, and further-

more the differences between $[\bar{A}(t)]$ for successive intervals are small. This is demonstrated by Figure 5, in which a representative component of $[\bar{A}(t)]$ from interval \mathcal{T}_0 is overlaid on the same component of $[A(t)]$ for interval \mathcal{T}_1 , and there is still close agreement.

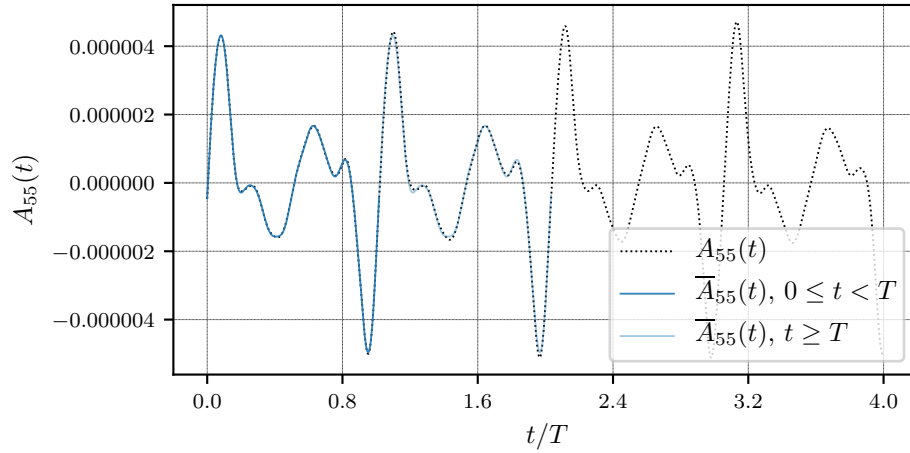


Figure 5: Select Component of Plant Matrix, $\Gamma = 3$, $[\bar{A}(t)]$ Computed from Interval \mathcal{T}_0

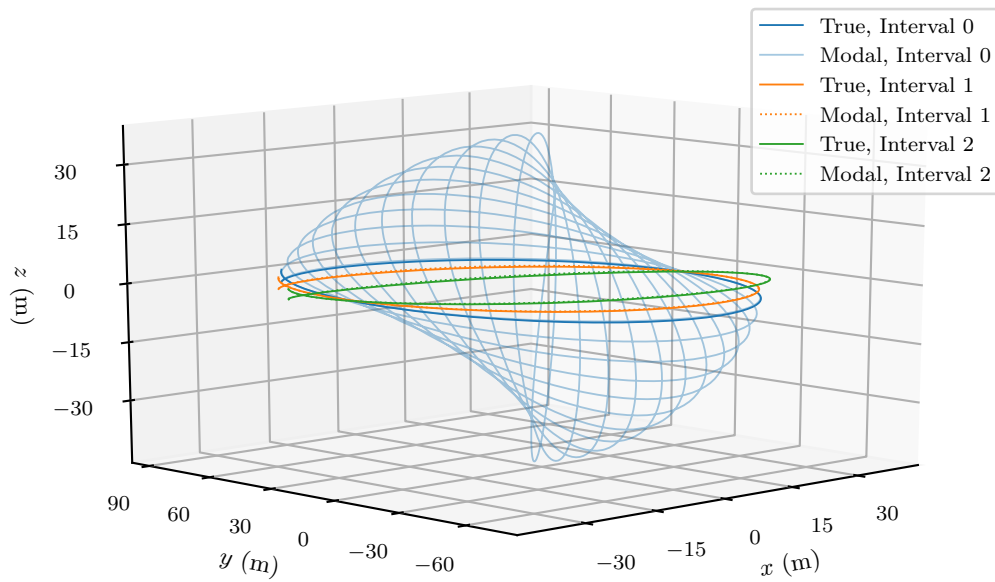


Figure 6: Relative Motion for Selected Mode, $\Gamma = 3$

Finally, Figure 6 demonstrates that the linearized modes computed in each interval are followed by the true uncontrolled relative motion dynamics, and the change of modal initial conditions between intervals is small. The characteristic modal motion predicted from interval \mathcal{T}_0 is reproduced in light blue, and is closely followed for one chief orbit by the nonlinear dynamics, represented in dark blue. There is actually close agreement between the two trajectories for many orbits, but only one orbit from the nonlinear dynamics is shown to avoid cluttering the plot. The plot also shows one orbit each of the modal prediction and nonlinear dynamics for the same mode computed in intervals \mathcal{T}_1 and \mathcal{T}_2 . The initial conditions are on the left edge of the plot, and the resulting trajectories are

clockwise if viewed from the $+z$ direction. While Figure 4(b) showed that the characteristic shape of the selected mode does not change significantly across intervals, Figure 6 shows that in addition, the difference between the modal initial conditions is only a few meters from interval to interval.

In a control implementation, the linearly predicted mode would serve as the guidance solution for the formation to follow. Multiple close-proximity spacecraft could safely occupy modal structures of the type depicted in Figure 4(b), either through a phasing difference or by targeting different scalings of the motion, since the structure is nearly scale-invariant in the linear regime of orbit element differences. This would enable close-proximity relative motion of many spacecraft despite the highly complex orbital dynamics. However, the trajectories eventually come close to the chief, so before that time the other spacecraft would have to reconfigure and target a new modal motion.

CONCLUSIONS

This paper develops a new analytic perspective and new numerical tools for spacecraft relative motion guidance in close proximity in quasi-periodic orbits in highly perturbed environments. For relative motion dynamics in applicable orbits, the periodic part of the time-varying plant matrix for relative motion dynamics is sampled over a quasi-period via Fourier transformations, and used to obtain modal decompositions in a transformed space for which the dynamics are linear time-invariant (LTI). The state error introduced by this process is studied analytically, and conditions for it to remain small are discussed. Then, a simple preliminary guidance implementation using these new results is outlined.

The primary theoretical arguments introduced in the paper are tested by application to high-fidelity simulations of spacecraft orbits and spacecraft formation flying about the asteroid Ryugu. The orbit studied is a perturbed terminator orbit with a quasi-period that is three times the rotation period of Ryugu. This demonstrates an example of robust relative motion modes that change only slowly, and the predicted modal relative motion is well-followed by the nonlinear dynamics. Additionally, an analysis using the relative motion dynamics with only the J_2 perturbation shows that the arguments used in this paper can be applied not only to quasi-periodic orbits, but more widely to slowly varying perturbed orbits as well, with insightful dynamical insight for these cases recoverable by such an analysis. The numerical work for this analysis is done in differential quasi-nonsingular (QNS) elements, but results are presented in LVLH coordinates for geometric clarity. The developments in this paper present new prospects for perturbed spacecraft relative motion control, offering an approach for approximating and studying perturbed relative motion in a variety of circumstances, from periodic or quasi-periodic orbits to slowly varying perturbed orbits.

REFERENCES

- [1] Kyle T. Alfriend, Hanspeter Schaub, and Dong-Woo Gim. Gravitational perturbations, nonlinearity and circular orbit assumption effect on formation flying control strategies. In *Proceedings of the Annual AAS Rocky Mountain Conference*, pages 139–158, Breckenridge, CO, Feb. 2–6 2000.
- [2] Carles Araguz, Elisenda Bou-Balust, and Eduard Alarcon. Applying autonomy to distributed satellite systems: Trends, challenges, and future prospects. *Systems Engineering*, 21(5):401–416, 2018.
- [3] Nicola Baresi. Bounded relative motion under zonal harmonics perturbations. *Celestial Mechanics and Dynamical Astronomy*, 127:527–548, 2017.
- [4] Nicola Baresi, Daniel J. Scheeres, and Hanspeter Schaub. Bounded relative orbits about asteroids for formation flying and applications. *Acta Astronautica*, 123:364 – 375, 2016.
- [5] W. Boyce. Comment on a Formula for the Gravitational Harmonic Coefficients of a Triaxial Ellipsoid. *Celestial Mechanics and Dynamical Astronomy*, 67(2):107–110, 1997.

- [6] S. B. Broschart and B. Villac. Identification of Non-Chaotic Terminator Orbits near 6489 Golevka. In *AAS/AIAA Spaceflight Mechanics Meeting*. American Astronautical Society, 2009.
- [7] Stephen B. Broschart, Gregory Lantoine, and Daniel J. Grebow. Quasi-terminator orbits near primitive bodies. *Celestial Mechanics and Dynamical Astronomy*, 120:195–215, 2014.
- [8] E. R. Burnett and E. A. Butcher. Linearized Relative Orbital Motion Dynamics in a Rotating Second Degree and Order Gravity Field, AAS 18-232. *Advances in the Astronautical Sciences*, 167:3463–3482, 2018.
- [9] Ethan R. Burnett and Hanspeter Schaub. Spacecraft Formation and Orbit Control Using Attitude-Dependent Differential Solar Radiation Pressure. *Advances in Space Research*, 2020.
- [10] Ethan R. Burnett and Hanspeter Schaub. Study of highly perturbed spacecraft formation dynamics via approximation. *Advances in Space Research*, 2020.
- [11] W. H. Clohessy and R. S. Wiltshire. Terminal Guidance System for Satellite Rendezvous. *Journal of the Aerospace Sciences*, 27(9):653–658, Sept. 1960.
- [12] D. J. Scheeres et al. Comparing the Estimated Dynamical Environments and Mass Distributions of Bennu and Ryugu. In *Asteroid Science*, 2019.
- [13] Gianluca Benedetti et al. Interplanetary CubeSats for asteroid exploration: Mission analysis and design. *Acta Astronautica*, 154:238–255, 2019.
- [14] S. Watanabe et al. Hayabusa2 arrives at the carbonaceous asteroid 162173 Ryugu—A spinning top-shaped rubble pile. *Science*, 364(6437):268–272, April 2019.
- [15] Dong-Woo Gim and Kyle T. Alfriend. The state transition matrix of relative motion for the perturbed non-circular reference orbit. *AIAA Journal of Guidance, Control, and Dynamics*, 26(6):956–971, 2003.
- [16] Tommaso Guffanti and Simone D’Amico. Linear Models for Spacecraft Relative Motion Perturbed by Solar Radiation Pressure. *Journal of Guidance Control, and Dynamics*, 42(9):1962–1980, 2019.
- [17] W. Hu and D. J. Scheeres. Numerical determination of stability regions for orbital motion in uniformly rotating second degree and order gravity fields. *Planetary and Space Science*, 52:685–692, 2004.
- [18] Jean Albert Kechichian. The analysis of the relative motion in general elliptic orbit with respect to a dragging and precessing coordinate frame. In *AAS/AIAA Astrodynamics Specialist Conference*, Sun Valley, Idaho, August 1997. Paper No. 97-733.
- [19] Paulett C. Liewer, Andrew T. Klesh, Martin W. Lo, Neil Murphy, Robert L. Staehle, Vassilis Angelopoulos, Brian D. Anderson, Manan Arya, Sergio Pellegrino, James W. Cutler, E. Glenn Lightsey, and Angelos Vourlidis. *A Fractionated Space Weather Base at L5 using CubeSats and Solar Sails*, pages 269–288. Springer Berlin Heidelberg, Berlin, Heidelberg, 2014.
- [20] Bharat Mahajan, Srinivas R. Vadali, and Kyle T. Alfriend. State-Transition Matrix for Satellite Relative Motion in the Presence of Gravitational Perturbations. *Journal of Guidance, Control, and Dynamics*, 42(7):1441–1457, 2019.
- [21] Robert G. Melton. Time-explicit representation of relative motion between elliptical orbits. *AIAA Journal of Guidance, Control, and Dynamics*, 23(4):604–610, 2000.
- [22] Yuri M. Nechepurenko. Bounds for the Matrix Exponential Based on the Lyapunov Equation and Limits of the Hausdorff Set. *Zhurnal Vychislitel’noi Matematiki i Matematicheskoi Fiziki*, 42(2):131–141, 2002.
- [23] Hanspeter Schaub and Kyle T. Alfriend. J_2 Invariant Relative Orbits for Spacecraft Formations. *Celestial Mechanics and Dynamical Astronomy*, 79(2):77–95, 2001.
- [24] Hanspeter Schaub and John L. Junkins. *Analytical Mechanics of Space Systems*. AIAA Education Series, Reston, VA, 4th edition, 2018.
- [25] D. J. Scheeres. Orbit Mechanics About Asteroids and Comets. *Journal of Guidance, Control, and Dynamics*, 35(3):987–997, May 2012.
- [26] D. J. Scheeres and F. Marzari. Spacecraft dynamics in the vicinity of a comet. *Journal of the Astronautical Sciences*, 50(1):35–52, January 2002.
- [27] J. Tschauner and P. Hempel. Rendezvous zu einem in elliptischer bahn umlaufenden ziel. *Astronautica Acta*, 11(5):104–109, 1965.
- [28] K Yamanaka and F. Ankersen. New State Transition Matrix for Relative Motion on an Arbitrary Elliptical Orbit. *AIAA Journal of Guidance, Control, and Dynamics*, 25(1):60 – 66, Jan. – Feb. 2002.